 doi:10.20944/preprints202108.0285.v1

Analysis of tilt effect on notch depth profiling using thin-skin regime of driver-pickup eddy-current sensor

Mingyang Lu [1,*,+], Xiaobai Meng [1,2*,+], Ruochen Huang [1], Anthony Peyton[1], Wuliang Yin [1,*]

[1] School of Electrical and Electronic Engineering, University of Manchester, Sackville Street Building, Manchester, M13 9PL, United Kingdom; mingyang.lu@manchester.ac.uk (M.L.); ruochen.huang@manchester.ac.uk (R.H.); a.peyton@manchester.ac.uk (A.P.); wuliang.yin@manchester.ac.uk (W.Y.)

[2] Faculty of Art, Science and Technology, University of Northampton, Northampton, NN1 5PH, United Kingdom; xiaobai.meng@northampton.ac.uk (X.M.)

* Correspondence: mingyang.lu@manchester.ac.uk (M.L.); wuliang.yin@northampton.ac.uk (W.Y.)

+ M.L. and X.M. contributed equally and share the first authorship.

Abstract: Electromagnetic eddy current sensors are commonly used to identify and quantify the surface notches of metals. However, the unintentional tilt of eddy current sensors affects results of size profiling, particularly for the depth profiling. In this paper, based on the eddy current thin-skin regime, a revised algorithm has been proposed for the analytical voltage or impedance of a tilted driver–pickup eddy current sensor scanning across a long ideal notch. Considering the resolution of the measurement, the bespoke driver–pickup, also termed as transmitter-receiver (T-R) sensor is designed with a small mean radius of 1 mm. Besides, the T-R sensor is connected to the electromagnetic instrument and controlled by a scanning stage with high spatial travel resolution , with a limit of 0.2 μm and selected as 0.25 mm. Experiments have been out on the voltage imaging of an aluminium sheet with 7 machined long notches of different depths using T-R sensor under different tilt angles. By fitting the measured voltage (both real and imaginary part) with proposed analytical algorithms, the depth profiling of notches is less affected by the tilt angle of sensors. From the results, the depth of notches can be retrieved within a deviation of 10 % for tilt angles up to 60 degrees.

Keywords: Eddy current driver–pickup sensor; surface crack; depth measurement; thin-skin regime; non-destructive testing.

1. Introduction

Based on the electromagnetic induction method, the eddy current testing (ECT) has been widely implemented for interrogating conductive structures [1-9]. Compared to other non-destructive techniques, ECT has merits of high adaptability and sensitivity, which applies to the property measurement and inspection of structural integrity [10-19]. For the measurement of defects in conductive structures, ultrasonic testing is reliable on identifying and locating (deep) defect clusters but hampered from the defect shielding [20]. In contrast, ECT is more efficient in quantifying surface notches, particularly for the depth of defect or rolling contact fatigue (RCF) [21] in rails.

Various methods have been used to analyse the response of eddy current inspecting notches, including numerical models such as Finite-element (FE) and boundary element (BE) model models, and eddy current thin-skin analytical method. For the numerical FE model, based on Maxwell equations with boundary conditions, the A-V form Galerkin equation has been proposed for field computations, including the field of magnetic vector potential A and electric scalar potential V [22].

Preprints (www.preprints.org) | NOT PEER-REVIEWED | Posted: 13 August 2021 doi:10.20944/preprints202108.0285.v1

By putting mesh information of all discretised subdomains together, the problem becomes finding the solution of equations with sparse stiffness matrix. Techniques have been proposed for hastening the solving process using FE A-V form Galerkin methods, including polishing the sparse stiffness matrix - the re-ordering and incomplete LU decomposing, optimised initial preconditioner, perturbed matrix, and weakly coupled effect [8,19,23-25]. Besides, other FE models including the use of reduced magnetic vector potential [26] and alternating current field measurement (ACFM) [27] have been utilised to calculate the field and sensor response. For the BE model, Theodoulidis, Poulakis, and Dragogias have proposed an improved method for accelerating the computation of impedance for the eddy current sensor scanning over narrow cracks [28]. For the analytical method, the eddy current thin-skin regime has been proposed to approximate the impedance for the eddy current sensor scanning over long notches [29,32]. The thin-skin method is based on the single-coil setup under high working frequencies, which is valid for the crack depth and length at least three times the eddy current skin depth.

Sensor tilt is identified as one of the major sources of noise in eddy-current surface inspections [29]. In this paper, to address the unintentional tilt effect on depth profiling of notches, a revised thin-skin algorithm for tilted T-R sensor scanning across the notch has been proposed. To increase the measurement resolution, the coil of sensor is wound with a small mean radius of 1 mm. Experimental measurements have been carried out for the voltage mapping of the T-R sensor scanning over cracks of an aluminium sheet under different tilt angles. To ensure that the thin-skin regime is applicable, notches are machined substantially long and deep. By referring to the diagram of voltage (both real and imaginary part) versus tilt angles, the depth of notches is retrieved despite of tilt effects.

2. Thin-skin regime using eddy-current T-R sensor

2.1. Original method - general formulas of thin-skin regime for self-impedance of tilted coil winding above long surface crack

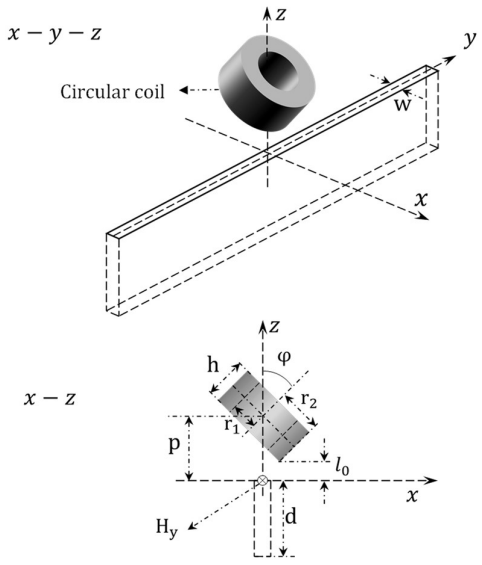

Figure 1. Tilted cross-sectional eddy-current air-core winding above an ideal notch of conductive half-space

The 3-D problem of a tilted cross-sectional eddy-current air-core coil winding above a long surface crack slot of conductive half-space [29] is shown in Fig. 1. The sensor rotates with respect to y axis with an angle of φ. Referring to [29], by applying the Fourier transform of the magnetic field in the normal space - Cartesian coordinate system, the magnetic field intensity generated from a tilted circular coil in the region $0 \le z \le l_0$ above the conductive half-space without crack is

Preprints (www.preprints.org) | NOT PEER-REVIEWED | Posted: 13 August 2021 doi:10.20944/preprints202108.0285.v1

$$\mathbf{H}(x,y,z)=\frac{\mathrm{I}}{2\pi}\int_{-\infty}^{\infty}\int_{-\infty}^{\infty}\frac{\mathrm{e}^{\mathrm{j}(\beta \mathrm{h}+ux+vy)}\tilde{h}(u,v)}{\alpha}(\mathrm{e}^{\alpha z}-\Phi\mathrm{e}^{-\alpha z})(\mathrm{j}u\hat{\mathbf{x}}+\mathrm{j}v\hat{\boldsymbol{y}})+(\mathrm{e}^{\alpha z}+\Phi\mathrm{e}^{-\alpha z})\hat{\mathbf{z}}\mathrm{d}u\,\mathrm{d}v \tag{1}$$

I is the excitation current flowing in the coil. j is the imaginary unit, which is expressed as the square root of -1. Besides, for the region $z \leq 0$ - inside the conductive half-space without crack, the magnetic field intensity becomes

$$\mathbf{H}(x,y,z)=\frac{\mathrm{I}}{2\pi}\int_{-\infty}^{\infty}\int_{-\infty}^{\infty}\frac{\mathrm{e}^{\mathrm{j}(\beta \mathrm{h}+ux+vy+\alpha_1 z)}\tilde{h}(u,v)(1-\Phi)}{\alpha}(\mathrm{j}u\hat{\mathbf{x}}+\mathrm{j}v\hat{\boldsymbol{y}}+\alpha_1\hat{\mathbf{z}})\mathrm{d}u\,\mathrm{d}v \tag{2}$$

In (1) and (2), h is the height of coil winding. x, y, and z are axial parameters in the Cartesian coordinate system. When the test piece is non-magnetic conductive material, B and α_1 are defined as

$$\beta = u\sin\varphi + \mathrm{j}\alpha\cos\varphi \tag{3}$$

$$\alpha_1 = \sqrt{\alpha^2 + \mathrm{j}2\pi\sigma\mu_0 \mathrm{f}} \tag{4}$$

σ is the electrical conductivity of test piece. μ_0 is the vacuum magnetic permeability. f is the operation frequency of excitation currents. α is the root mean square of 2-D Fourier variables - u and v, which is related to the wavenumber of Transverse (TE) plane waves [25].

$$\alpha = \sqrt{u^2+v^2} \tag{5}$$

In (1) and (2), $\tilde{h}(u,v)$ is the 2-D Fourier transform of the free-space magnetic field incident on $z=0$ at x-y plane for a unit ampere of the excitation current, which is sensor dependent. For a cross-sectional coil winding, $\tilde{h}(u,v)$ is defined as

$$\tilde{h}(u,v) = \mathrm{j}\frac{\mathrm{N}}{\mathrm{h}(\mathrm{r}_2-\mathrm{r}_1)}\frac{\mathrm{M}}{\beta^3}\mathrm{e}^{-\alpha \mathrm{p}}\sin\left(\frac{\beta \mathrm{h}}{2}\right) \tag{6}$$

r_1 and r_2 are the inner and outer radius of coil windings, N is the turn number of coil windings. As shown in Fig. 1, p and l_0 are the lift-off distance from the centre and bottom of the tilted sensor to the test piece($\mathrm{p} = l_0 + \mathrm{r}_2\sin|\varphi|$). M is the integral related to the first-order modified Bessel term I_1.

$$\mathrm{M} = \int_{\beta \mathrm{r}_1}^{\beta \mathrm{r}_2} \tau \mathrm{I}_1(\tau)\mathrm{d}\tau \tag{7}$$

To speed up the computation, the integration in (7) can be expanded as

$$\mathrm{M} = \frac{\pi\beta}{2}\{\mathrm{r}_1[\mathrm{I}_0(\beta \mathrm{r}_1)\mathbf{L}_1(\beta \mathrm{r}_1) - \mathrm{I}_1(\beta \mathrm{r}_1)\mathbf{L}_0(\beta \mathrm{r}_1)] - \mathrm{r}_2[\mathrm{I}_0(\beta \mathrm{r}_2)\mathbf{L}_1(\beta \mathrm{r}_2) - \mathrm{I}_1(\beta \mathrm{r}_2)\mathbf{L}_0(\beta \mathrm{r}_2)]\} \tag{8}$$

I_n and $\mathbf{L}_n$ are the first-kind modified Bessel and Struve functions with order n. Empirically, according to [30], Φ is a material-dependent term and defined as

$$\Phi = \frac{(\alpha_1+\alpha)(\alpha_1-\alpha) - (\alpha_1+\alpha)(\alpha_1-\alpha)\mathrm{e}^{2\alpha_1 \mathrm{c}}}{-(\alpha_1-\alpha)(\alpha_1-\alpha) + (\alpha_1+\alpha)(\alpha_1+\alpha)\mathrm{e}^{2\alpha_1 \mathrm{c}}} \tag{9}$$

c is the thickness of test pieces. Assume the depth and gape of the long surface crack are d and w respectively. Considering the thin-skin depth regime of thick non-magnetic plates, the frequency of the current must large enough that the crack depth d and length are at least three times skin depths [31,32]. As $\mathrm{c} \gg \mathrm{d}$, the sample can be treated as a non-magnetic conductive half-space. Besides, Φ can be approximated as

Preprints (www.preprints.org) | NOT PEER-REVIEWED | Posted: 13 August 2021 doi:10.20944/preprints202108.0285.v1

$$\Phi = \frac{\alpha - \alpha_1}{\alpha + \alpha_1} \tag{10}$$

Referring to [29], according to the boundary condition - where the normal component of **H** is continuous at different material interfaces, the impedance change caused by long notches of the half-space conductor using a single tilted coil is

$$\Delta Z_c = \mu_0 f \int_{-\infty}^{\infty} \frac{g(w)}{1 + \frac{2v\tilde{U}\tanh(vd)}{jk}} \frac{\tilde{H}_y(-v)\tilde{H}_y(v)}{v^2} dv \tag{11}$$

In (11), $g(w)$ is a parameter dependent on the crack gape. Parameters - $g(w)$, k, $\tilde{U}$ (even functions of v) are defined in the appendix.

$\tilde{H}_y(v)$ is related to the Fourier transform of H_y for a unit ampere of the excitation current. H_y is the source contribution of the magnetic field intensity, which is approximated by $\mathbf{H}(x, y, z)$ at (0,0,0) along y axis without the crack [29].

$$\tilde{H}_y(v) = v \int_{-\infty}^{\infty} \tilde{h}(u, v) \frac{\alpha_1}{a(\alpha + \alpha_1)} du \tag{12}$$

Besides, the impedance change for the non-magnetic half-space conductor without defect is

$$Z_0 = j4\pi\mu_0 If \int_{-\infty}^{\infty} \int_{-\infty}^{\infty} \frac{\tilde{h}(-u, -v)\tilde{h}(u, v)(\alpha - \alpha_1)}{\alpha(\alpha + \alpha_1)} du\, dv \tag{13}$$

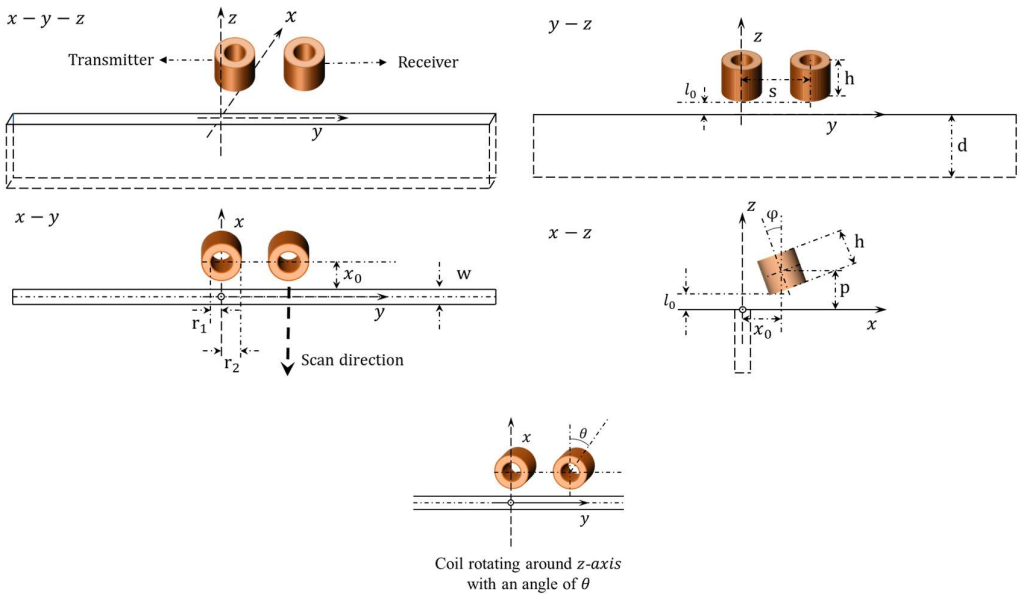

Figure 2. Tilted eddy current T-R sensor scanning across (x direction) and through the centre of a long surface crack slot on the conductive half-space.

2.2. Method - Revised algorithms of mutual impedance of tilted T-R sensor scanning cross long notches

In Fig. 2, the T-R sensor, also termed as the driver-pickup sensor, is used for the notch depth profiling on non-magnetic metals. The transmitter and receiver are tilted - rotating with crack

Preprints (www.preprints.org) | NOT PEER-REVIEWED | Posted: 13 August 2021 doi:10.20944/preprints202108.0285.v1

direction – $y\text{-}axis$ at the same lift-off plane (l_0), with a horizontal separation distance of s. Parameters of the T-R sensor are listed in Table 1.

Assume the scan direction of tilted T-R sensor is perpendicular to the crack orientation, x_0 is the transient distance to the crack. For the transmitter, $\widetilde{H}_y(v)$, H component along y axis, is related to H_y at $(x_0, 0,0)$ without the crack. Thus, referring to (1) and (2), for the non-magnetic material, $\tilde{h}(u,v)$ becomes $\tilde{h}(u,v)e^{jux_0}$ when the transmitter shifted from $(0,0,p)$ to $(x_0,0,p)$.Consequently, $\widetilde{H}_y(v)$ for the transmitter becomes

$$\widetilde{H}_{yt}(v) = v\int_{-\infty}^{\infty}\frac{\tilde{h}(u,v)e^{jux_0}\alpha_1}{\alpha(\alpha+\alpha_1)}du \tag{15}$$

Besides, $\tilde{h}(u,v)$ becomes $\tilde{h}(u,v)e^{j(ux_0+vs)}$ when the receiver shifted from $(0,0,p)$ to (x_0,s,p). Thus, $\widetilde{H}_y(v)$ for the receiver becomes

$$\widetilde{H}_{yr}(v) = v\int_{-\infty}^{\infty}\frac{\tilde{h}(u,v)e^{j(ux_0+vs)}\alpha_1}{\alpha(\alpha+\alpha_1)}du \tag{16}$$

Then, the voltage change due to notches using the tilted T-R sensor is (referring to equation 11)

$$\Delta Z_c = \mu_0 f\int_{-\infty}^{\infty}\frac{g(w)}{1+\frac{2v\tilde{U}\tanh(vd)}{jk}}\frac{\widetilde{H}_{yt}(-v)\widetilde{H}_{yr}(v)}{v^2}dv \tag{17}$$

Thus, the voltage change due to the notch using the T-R sensor is

$$\Delta V_c(x_0) = \mu_0 If\int_{-\infty}^{\infty}\frac{g(w)}{1+\frac{2v\tilde{U}\tanh(vd)}{jk}}\frac{\widetilde{H}_{yt}(-v)\widetilde{H}_{yr}(v)}{v^2}dv \tag{18}$$

In (18), ΔV_c is the voltage change due to the secondary magnetic field from the eddy current affected by the defect of test piece. To mitigate the discrepancy between experimental and analytical data, the crack depth is retrieved by referring to the normalised version of (18) - $\frac{\Delta V_c(x_0)}{V_0}$. V_0 is the magnitude of the voltage change, which is nullified by the free space voltage to eliminate the mutual coupling effect of coils for the defect-free region of the non-magnetic plate. Referring to (13) and revised $\tilde{h}(u,v)$ for both the transmitter ($\tilde{h}(u,v)e^{jux_0}$) and receiver ($\tilde{h}(u,v)e^{j(ux_0+vs)}$), the modified V_0 for tilted T-R sensor is

$$V_0 = \left|j4\pi\mu_0 If\int_{-\infty}^{\infty}\int_{-\infty}^{\infty}\frac{\tilde{h}(-u,-v)\tilde{h}(u,v)(\alpha-\alpha_1)e^{jvs}}{\alpha(\alpha+\alpha_1)}\,du\,dv\right| \tag{19}$$

By fitting the normalised analytical voltage change $\frac{\Delta V_c(x_0)}{V_0}$ with the measured one for different tilt angles, the depth of notches is retrieved.

As shown in Fig. 2, for the case of coil windings rotating around $z\text{-}axis$ with an angle of θ, the free-space source term $\tilde{h}(u,v)$ is replaced with the following one.

$$\tilde{h}(u\cos\theta + v\sin\theta, -u\sin\theta + v\cos\theta) \tag{20}$$

Table 1. Parameters of the T-R eddy-current sensor and measurement setup.

Parameter	Transmitter coil

Preprints (www.preprints.org) | NOT PEER-REVIEWED | Posted: 13 August 2021 doi:10.20944/preprints202108.0285.v1

	or receiver coil
Inner radius r_1 (mm)	0.75
Outer radius r_2 (mm)	1.25
Turns N	300
Spacing s (mm)	3.0
Coil wire diameter (mm)	0.071
Coil height h (mm)	3.0
Lift-off l_0 (mm)	2.0
Tilt angle φ (degree)	0:10:60
Working frequency f (kHz)	300
Magnitude of free-space voltage (152 kHz) (V)	1.12
Driven current (mA rms)	48
Free-space coil inductance (H)	2.45×10^{-5}
Free-space coil DC resistance (Ω)	3.32×10^{-8}

Table 2. Parameters of the conductive samples with long surface notch.

Parameter		Value
Aluminium sheet	Electrical conductivity σ (MS/m)	36.9
	Relative permeability	1
	Thickness (mm)	2.0
	Magnitude of voltage change V_0 (mV) without surface notches under 300 kHz	225.7
	Skin depth (mm) under 300 kHz	0.15
Machined surface crack slot	Width/gape w (mm)	0.25
	Length (mm)	10.0
	Depth d (mm)	0.4:0.2:1.6

3. Experiments

As listed in Table 1, the transmitting and receiving coils are wound by enamelled copper wires. The coil windings are air-cored, with the coil wound on plastic rods by the coil winder machine. As shown in Fig. 3, the T-R sensor is connected to a bespoke electromagnetic (EM) instrument to map the voltage of the T-R sensor above specimen with machined notches. The EM instrument is fabricated by the SISP group at school of Electrical and Electronic Engineering, University of Manchester) [33-35]. The EM instrument is FPGA (Field Programmable Gate Array) based, which can achieve a data frame rate of 100 k/s. The EM instrument is connected to the PC through the Ethernet

Preprints (www.preprints.org) | NOT PEER-REVIEWED | Posted: 13 August 2021 doi:10.20944/preprints202108.0285.v1

cable. More details of the EM instrument (including specifications, operations, features) are reported in [33].

As illustrated in Fig. 4, the sensor is controlled by a C-programmable scanning stage (Newmark Systems Inc. USA). The scanning stage is composed of two control motors, with a travel resolution of 0.2 μm per step and travel limit of 200 mm. The scanning speed of stage is 100 mm/s. For the inspection of test piece, as listed in Table 2, the travel resolution is selected as 0.25 mm. To achieve a relatively high sensitivity of the voltage mapping, the transmitter and receiver of T-R sensor are aligned with crack orientation during the scanning. In Fig. 4, a misalignment of the sensor to the crack results in a reduced sensitivity of voltage mapping. As exhibited in table 2 and Fig. 4, the aluminium sheet contains seven machined notches with identical length and gape but different depths. To ensure that the thin-skin regime valid and can be applied to the machined cracks, the (upgraded version of) EM instrument is operated under the working frequency of 300 kHz. Thus, the skin depth of the induced eddy current is 0.15 mm, which substantially smaller than the depth of the machined slot (with a minimum depth of 0.4 mm, as shown in Table 2).

The eddy current is designed as driver–pickup or T-R sensor instead of single or co-axial sensor, which is verified to having a higher spatial resolution, which doubles the resolution of single-coil sensor with the same size [36], wider frequency range, higher gain, and being barely affected by the thermal drift [37]. Moreover, as shown in Table 1, the mean radius of the coil winding is only 1 mm, which achieves a relatively high sensitivity on the voltage mapping of notches.

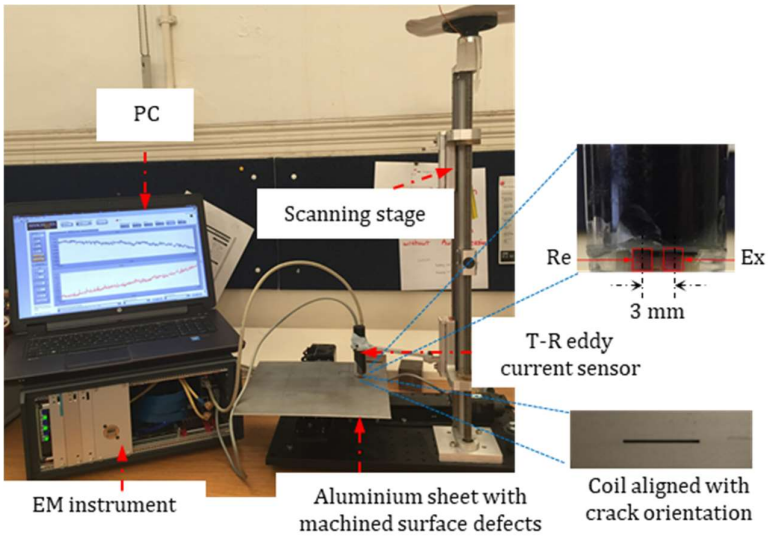

Figure 3. Experimental setup for electromagnetic imaging of surface cracks using T-R eddy current sensor.

Preprints (www.preprints.org) | NOT PEER-REVIEWED | Posted: 13 August 2021 doi:10.20944/preprints202108.0285.v1

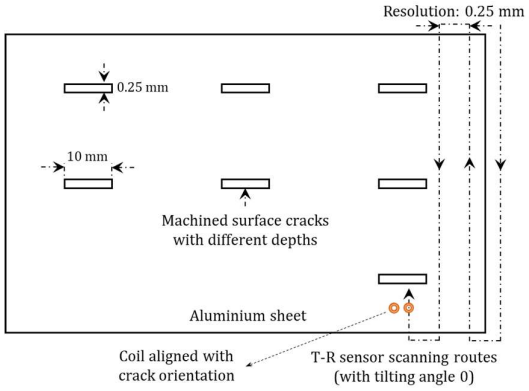

Figure 4. Scanning route of tilted T-R sensor for electromagnetic imaging of aluminium sheet with machined surface slots of different depths.

4. Result and discussion

4.1. Scanned voltage for T-R sensor across notch without tilt effect

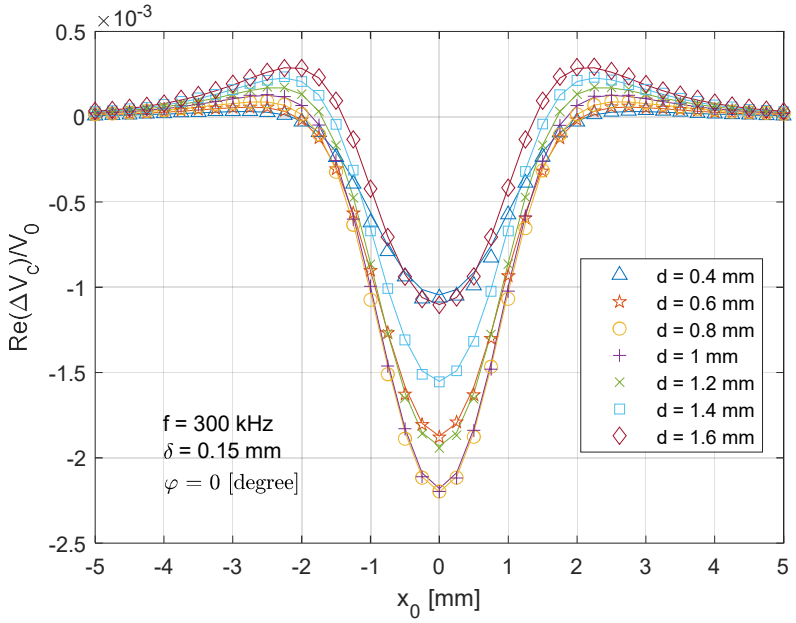

Figure 5. Comparison of analytical (lines) and experimental (markers) results for the real part of normalised voltage change (due to the crack) for T-R sensor (tilt angle $\varphi = 0$ degree) scanning across (x direction in Fig. 2) and through the crack centre

Fig. 5 depicts the comparison between the theoretical (solid lines) and measurement (markers) data of the real part of the normalised voltage change ($\frac{\mathrm{Re}(\Delta V_c(x_0))}{V_0}$) when the T-R sensor (tilt angle $\varphi = 0$ degree) scans across the centre of the crack from ($x_0 = -5$ mm in Fig. 2) to ($x_0 = 5$ mm) with a travelling step of 0.25 mm. It can be observed that the theoretical/analytical result fits well with the measurement, with a maximum error around 4.4 %. The sensor response (normalised voltage change) reaches its maximum magnitude when $x_0 = 0$ mm, where the T-R sensor is above the centre of the crack with a lift-off distance of 2 mm. As the T-R sensor drifts away, the T-R sensor less interacts with

Preprints (www.preprints.org) | NOT PEER-REVIEWED | Posted: 13 August 2021 doi:10.20944/preprints202108.0285.v1

the test piece, which results in the attenuated (normalised) voltage change due to the crack. For $x_0 = \pm 2$ mm, an overshoot is observed. Besides, a deeper surface slot results in a higher amplitude of the real part of voltage change. Besides, it can be found in Fig. 5 that, a slightly deeper crack slot results in a higher magnitude for the real part of voltage change due to the crack. However, a further deeper crack will result in reduced signal magnitude. Intuitively, a deeper surface crack results in a higher amplitude of voltage change magnitude. However, the phase of voltage change varies with increased crack depth and different sensor positions (x_0). Thus, for some sensor positions, the real part of the voltage change does not monotonically increase with the crack depth. That's why for the position $x_0 = 0$ mm, the results of d = 0.4 mm and d = 1.6 mm are quite similar, while for the position $x_0 = \pm 2$ mm, the results of d = 0.4 mm and d = 1.6 mm are different.

In Fig. 6, a similar symmetric trend can be found at the imaginary part of normalised voltage change ($\frac{\mathrm{Im}(\Delta V_C(x_0))}{V_0}$) when the T-R sensor scans across the centre of the crack with the same path in Fig. 5. The maximum error between the analytical and experimental data is around 5.3 %. Since the test piece becomes more inductive under high working frequencies (referring to [38-44]), the magnitude for the imaginary part of voltage changes due to the crack is much larger than (around 20 times) that of the real part. Owing to the different sensitivity, a deeper crack results in a larger magnitude of voltage change. This is because the imaginary part dominates the magnitude of the voltage change, which increase with the depth of surface crack. Besides, compared to the real part in Fig. 5, less overshoot can be observed from the imaginary part in Fig. 6. More sensitivity analyses are reported in [28].

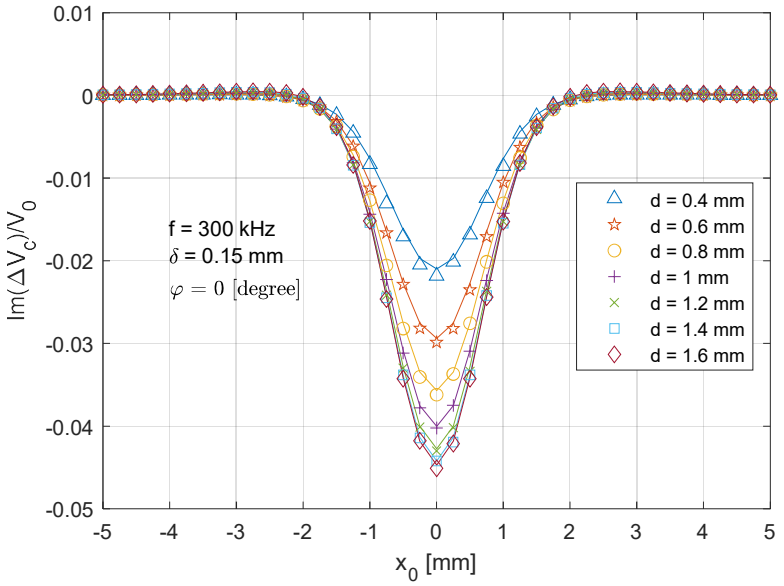

Figure 6. Comparison of analytical (lines) and experimental (markers) results for the imaginary part of normalised voltage change (due to the crack) for T-R sensor (tilt angle φ = 0 degree) scanning across (x direction in Fig. 2) and through the crack centre

Preprints (www.preprints.org) | NOT PEER-REVIEWED | Posted: 13 August 2021 doi:10.20944/preprints202108.0285.v1

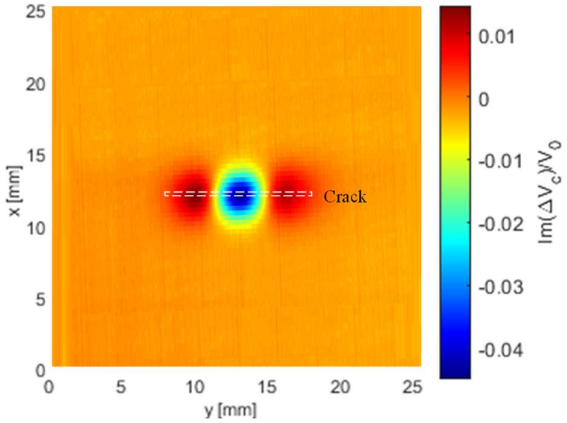

Figure 7. 2-D imaging of the imaginary part of normalised voltage change (due to the crack) using T-R sensor (tilt angle $\varphi = 0$ degree) for the inspection of surface notch with depth of 1.6 mm

Fig. 7 shows the 2-D voltage imaging for the imaginary part of normalised voltage changes of the crack slot (1.6 mm deep) using T-R sensor. The span of plot is 30 and 40 mm (and resolution of 0.25 mm in each travel step) in x and y directions. As can be observed from the 3-D version of (imaginary part) voltage change due to the crack in Fig. 8, two bumps and one hollow exist for T-R sensor with tilt angle $\varphi = 0$ degree scanning along the centre of notches in y direction. However, for T-R sensor scanning across the crack and through its centre, only one hollow can be observed at crack centre, which follows the same trend in Fig. 6.

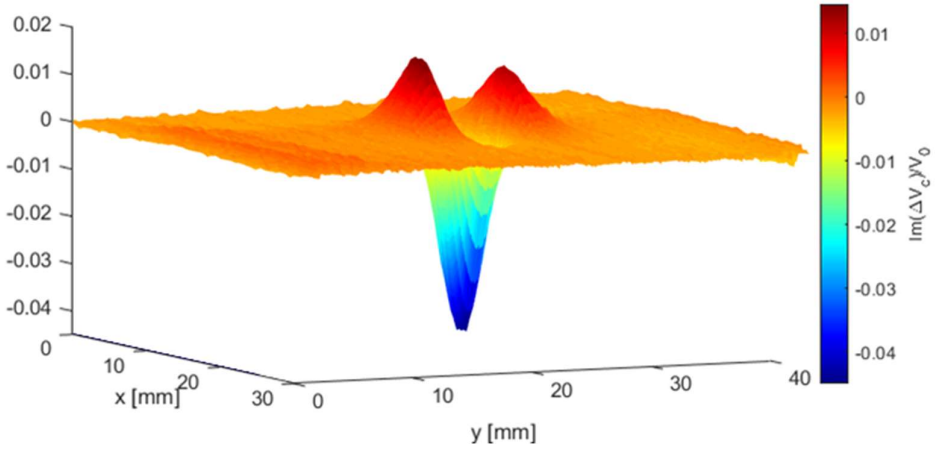

Figure 8. 3-D imaging of the imaginary part of normalised voltage change (due to the crack) using T-R sensor (tilt angle $\varphi = 0$ degree) for the inspection of surface notch with depth of 1.6 mm

Preprints (www.preprints.org) | NOT PEER-REVIEWED | Posted: 13 August 2021 doi:10.20944/preprints202108.0285.v1

4.2. B. Tilted T-R sensor across the crack

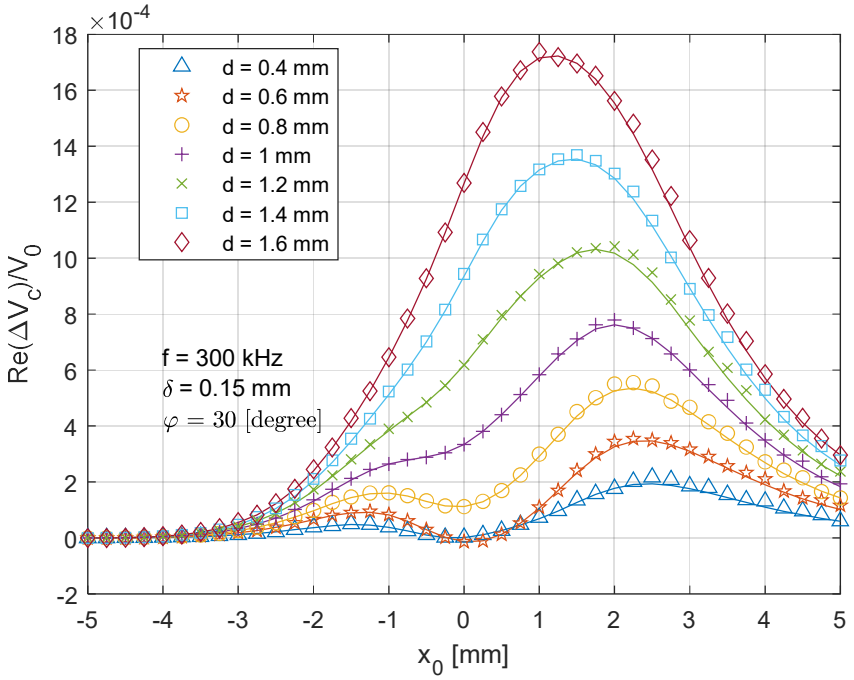

Figure 9. Comparison of analytical (lines) and experimental (markers) results for the real part of normalised voltage change (due to the crack) for T-R sensor (tilt angle φ = 30 degrees) scanning across (*x* direction in Fig. 2) and through the crack centre

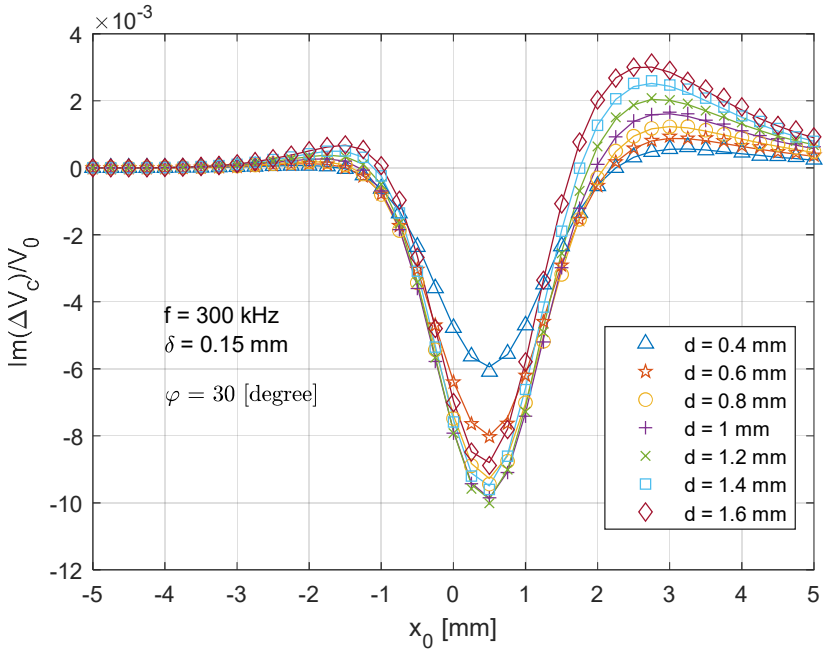

Figure 10. Comparison of analytical (lines) and experimental (markers) results for the imaginary part of normalised voltage change (due to the crack) for T-R sensor (tilt angle φ = 30 degrees) scanning across (*x* direction in Fig. 2) and through the crack centre

Preprints (www.preprints.org) | NOT PEER-REVIEWED | Posted: 13 August 2021 doi:10.20944/preprints202108.0285.v1

As shown in Fig. 9 and Fig. 10, when the T-R sensor rotates around the crack direction (y-$axis$ in Fig. 2) with an angle of 30 degrees, the scanned voltage for both real and imaginary part become asymmetric. The peak value point is slightly right shifted. Besides, the real part of the scanned voltage becomes positive-dominant. Moreover, a slight higher overshoot can be observed on the right side (around $x_0 = 2.5$ mm) of the imaginary voltage change.

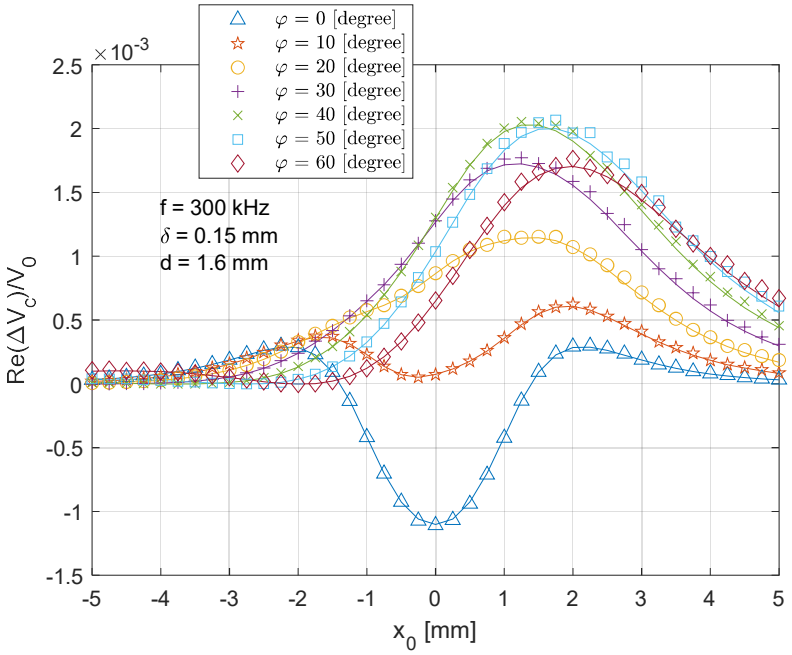

Figure 11. Comparison of analytical (lines) and experimental (markers) results for the real part of normalised voltage change (due to the crack) for T-R sensor scanning across (x direction in Fig. 2) and through the crack centre with the depth of 1.6 mm and different tilt angles

Fig. 11 and Fig. 12 show the real and imaginary part of the scanned voltage for different tilt angles when the T-R sensor scans across (x direction in Fig. 2) the crack centre with the depth of 1.6 mm. As the tilt angle increases, the real part of voltage changes gradually right shifts and becomes positive-dominant. For the imaginary part of voltage change, the curve in Fig. 12 also shifts right but significantly attenuates with the increased tilt angle, which is caused by the less interactive effect or coupling effect between the T-R sensor and defected area. As the primary magnetic field is lack of symmetry with respect to z-axis when the coils are tilted, the induced eddy current also becomes asymmetric [29]. As a result, the secondary magnetic field from the induced eddy current and the overall received signal from the probe become less symmetric with respect to the crack centre. Thus, the voltage curve in Fig. 11 and 12 becomes asymmetric with respect to the position $x_0 = 0$ mm. As explained regarding Fig. 5, the phase of voltage change varies with crack depth. Since the imaginary part dominates in the magnitude of voltage change, in Fig. 12, a deeper crack results in a higher overall amplitude of voltage change.

Preprints (www.preprints.org) | NOT PEER-REVIEWED | Posted: 13 August 2021 doi:10.20944/preprints202108.0285.v1

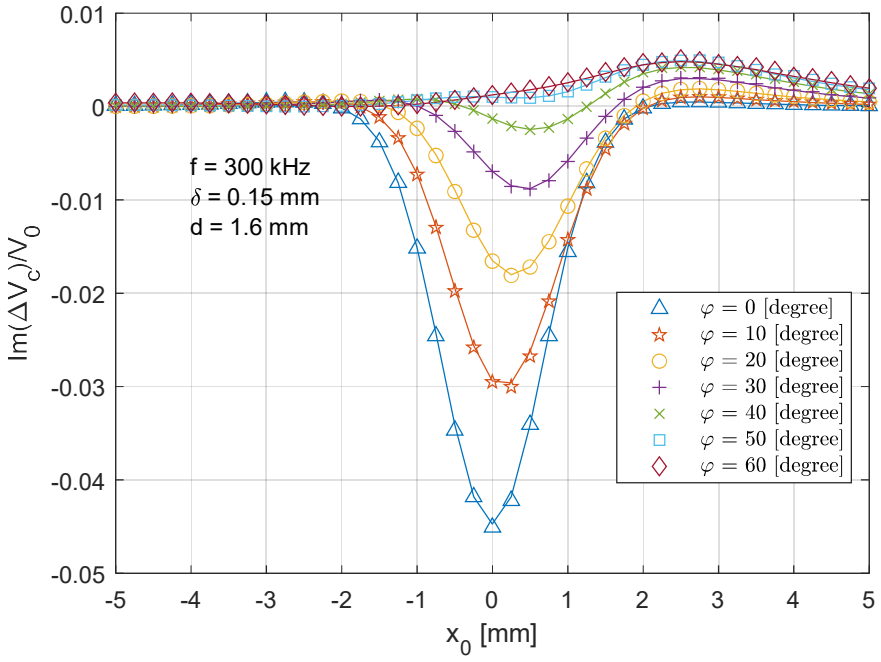

Figure 12. Comparison of analytical (lines) and experimental (markers) results for the imaginary part of normalised voltage change due to the crack for T-R sensor scanning across (x direction in Fig. 2) and through the crack centre with the depth of 1.6 mm and different tilt angles

4.3. Retrieval of surface crack depth

The voltage change for T-R sensor above the crack centre has a decent amplitude and sensitivity (particularly for a small tilt angles), which is used to retrieve the notch depth considering different tilt angles of T-R sensor. Fig. 13 and Fig. 14 depict the real part and imaginary part of the voltage change versus tilt angle of sensors at different crack depths. The analytical result exhibits a decent agreement with the measured one, with a maximum error of 4.1 % and 5.3 % for the depth of 0.4 mm case. Fig. 15 illustrates the retrieval of crack depth versus its actual value under different tilt angles. In Fig. 15, the blue dash line with a unit constant shows the ideal depth by means of dimensional measurement. Different markers depict the retrieved thickness from the proposed method at different tilt angles. Retrieval and measurement are conducted at crack depths from 0.4 mm to 1.6 mm with a uniform increment of 0.2 mm. The uncertainty of retrieved depth and depth by means of dimensional measurement is 0.02 mm and 0.01 mm. By altering the parameter d when fitting analytical value (both the real and imaginary part) of $\frac{\Delta V_c(x_0)}{V_0}$ (equation 18 and 19) with measured one, the deviation of notch depth profiling is controlled within 10 % for all the crack slots and tilt angles. The maximum deviation (9 %) of the retrieved depth occurs at crack depth of 0.4 mm with tilt angle of 60 degrees, where the crack depth is 2.67 times that of the skin depth (which is slightly below the criteria of thin-skin regime). Overall, it can be observed that a larger tilt angle results a large deviation of depth retrieval.

Preprints (www.preprints.org) | NOT PEER-REVIEWED | Posted: 13 August 2021 doi:10.20944/preprints202108.0285.v1

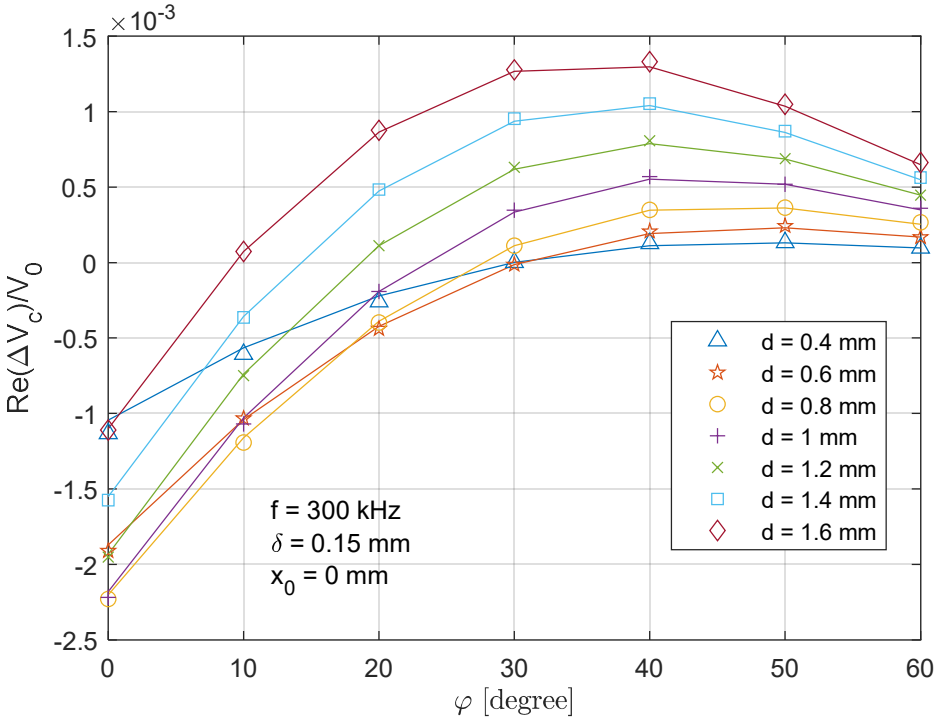

Figure 13. Comparison of analytical (lines) and experimental (markers) results for the real part of normalised voltage change (due to the crack) versus tilt angles when T-R sensor is above the crack centre ($x_0 = 0$ mm)

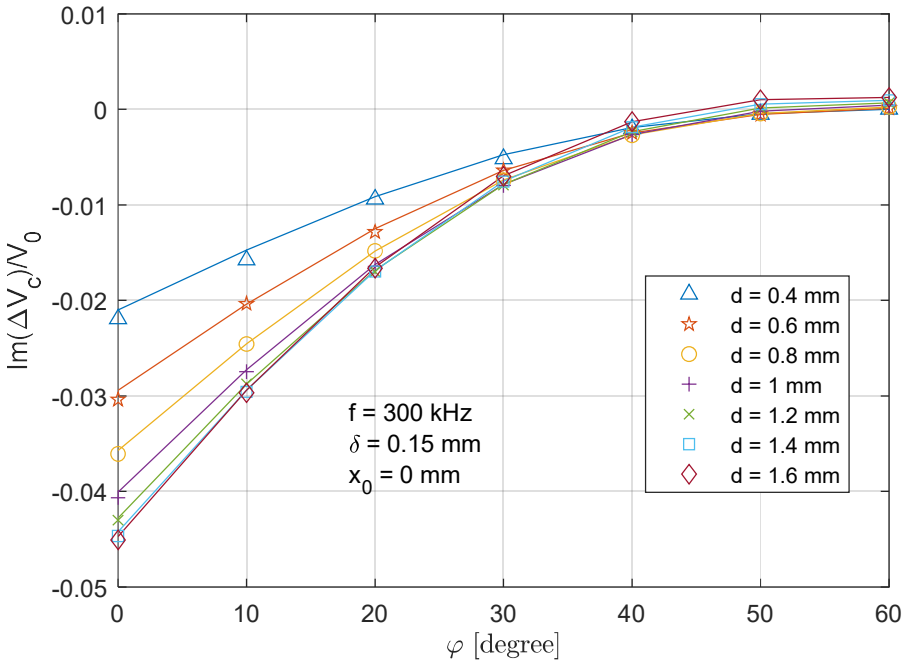

Figure 14. Comparison of analytical (lines) and experimental (markers) results for the imaginary part of normalised voltage change (due to the crack) versus tilt angles when T-R sensor is above the crack centre ($x_0 = 0$ mm)

Preprints (www.preprints.org) | NOT PEER-REVIEWED | Posted: 13 August 2021 doi:10.20944/preprints202108.0285.v1

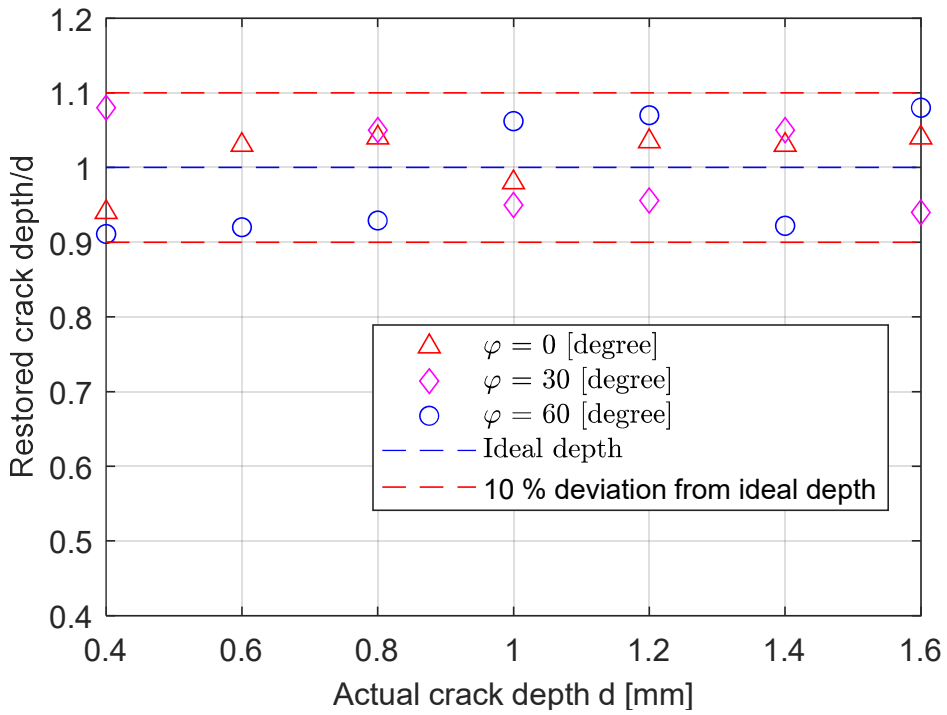

Figure 15. Retrieval of the surface crack slot versus actual depths for the tilt angle of 0, 30, and 60 degrees

5. Conclusions

In this paper, based on the thin-skin regime, an impedance or voltage algorithm for tilted T-R sensor scanning across notches has been proposed for the first time. By referring to both real and imaginary part of the diagram of voltage versus tilt angles, the depth of notches is retrieved despite of tilt effects. Experimental voltage imaging has been conducted for the eddy current T-R sensor scanning over notches on an aluminium sheet with different tilt angles - circumferential tilt regarding to crack orientation. From the result, the error of depth profiling for notches has been controlled within 10 %. However, the proposed method has merely analysed the circumferential tilt effect of the T-R sensor regarding to crack orientation ($\theta = 0$ in equation 20). The longitudinal tilt effect of T-R sensor on the notch depth profiling will be investigated in the future. Besides, the proposed algorithms are based on the non-ferrous metals. Further investigations of notches on ferrous steel will be carried out in the future.

Appendix:

Followings show the definition of parameters $g(\mathrm{w})$, k, and $\tilde{\mathrm{U}}$ in equation (11),

$$g(\mathrm{w}) = \mathrm{j}g_{\mathrm{f}}\mathrm{w} + (1+\mathrm{j})\delta\left(g_{\mathrm{f}} - \frac{g_{\mathrm{s}}\mathrm{w}}{2}\right) + \frac{g_{\mathrm{k}}\delta^2}{2} \tag{1}$$

δ is the skin depth function of the non-magnetic materials.

$$\delta = \sqrt{\frac{1}{\pi\sigma\mu_0 \mathrm{f}}} \tag{2}$$

In (1),

$$g_{\mathrm{f}} = v\tanh(v\mathrm{d}) \tag{3}$$

$$g_{\mathrm{s}} = \left[1 + \frac{2v}{\mathrm{j}k}\left(\tilde{\mathrm{U}} + \tilde{\mathrm{V}}\right)\tanh(v\mathrm{d}) - \mathrm{sech}(v\mathrm{d})\right]v^2 \tag{4}$$

$$g_{\mathrm{k}} = \left\{\mathrm{sech}(v\mathrm{d}) - \frac{8}{\pi}\left[1 + \frac{v}{\mathrm{j}k}\left(\tilde{\mathrm{U}} + \tilde{\mathrm{V}}\right)\tanh(v\mathrm{d}) - \mathrm{sech}(v\mathrm{d})\right]\right\}v^2 \tag{5}$$

In (5), $\tilde{\mathrm{U}}$ and $\tilde{\mathrm{V}}$ are even functions. For the non-magnetic materials, $\tilde{\mathrm{U}}$ and $\tilde{\mathrm{V}}$ are defined as,

$$\tilde{U} = \frac{1}{2\pi}\left[\frac{1}{\varepsilon}\ln\left(\frac{1+\varepsilon}{1-\varepsilon}\right) - \frac{1}{\sqrt{1+\varepsilon^2}}\ln\left(\frac{1+\sqrt{1+\varepsilon^2}}{1-\sqrt{1+\varepsilon^2}}\right)\right] \quad (6)$$

$$\tilde{V} = -\frac{1}{\pi}\ln\left(\frac{\varepsilon}{\sqrt{\varepsilon^2-1}}\right) \quad (7)$$

In (5), k is defined as,

$$k = \frac{-1+j}{\delta} \quad (8)$$

In (6) and (7),

$$\varepsilon = \frac{v}{k} \quad (9)$$

Author Contributions: Conceptualization, M.L. and X.M.; methodology, M.L. and X.M.; software, M.L. and X.M.; validation, M.L. and X.M.; formal analysis, M.L. and X.M.; data curation, X.M., M.L., R.H. and W.Y.; writing—original draft preparation, M.L. and X.M.; writing—review and editing, M.L. and X.M.; administration, M.L., A.P. and W.Y.; All authors have read and agreed to the published version of the manuscript.

Conflicts of Interest: The authors declare no conflict of interest.

References

1. Yang, G.; Dib, G.; Udpa, L.; Tamburrino, A.; Udpa, S.S. Rotating field EC-GMR sensor for crack detection at fastener site in layered structures. *IEEE Sensors Journal*, **2014**, *15*, 463-470.
2. Vasic, D.; Bilas, V.; Ambrus, D. Pulsed eddy-current nondestructive testing of ferromagnetic tubes. *IEEE transactions on instrumentation and measurement*, **2004**, *53*, 1289-1294.
3. Li, W.; Chen, G.; Ge, J.; Yin, X.; Li, K. High sensitivity rotating alternating current field measurement for arbitrary-angle underwater cracks. *NDT & E International*, **2016**, *79*, 123-131.
4. Egorov, A.V.; Polyakov, V.V.; Salita, D.S.; Kolubaev, E.A.; Psakhie, S.G.; Chernyavskii, A.G.; Vorobei, I.V. Inspection of aluminum alloys by a multi-frequency eddy current method. *Defence Technology*, **2015**, *11*, 99-103.
5. Lu, M.; Peyton, A.; Yin, W. Acceleration of frequency sweeping in eddy-current computation. *IEEE Transactions on Magnetics*, **2017**, *53*, 1-8.
6. Bowler, J.R.; Norton, S.J.; Harrison, D.J. Eddy-current interaction with an ideal crack. II. The inverse problem. *Journal of applied physics*, **1994**, *75*, 8138-8144.
7. Lu, M.; Xu, H.; Zhu, W.; Yin, L.; Zhao, Q.; Peyton, A.; Yin, W. Conductivity Lift-off Invariance and measurement of permeability for ferrite metallic plates. *NDT & E International*, **2018**, *95*, 36-44.
8. Lu, M.; Peyton, A.; Yin, W. Acceleration of frequency sweeping in eddy-current computation. *IEEE Transactions on Magnetics*, **2017**, *53*, 1-8.
9. Avila, J.R.S.; Lu, M.; Huang, R.; Chen, Z.; Zhu, S.; Yin, W. Accurate measurements of plate thickness with variable lift-off using a combined inductive and capacitive sensor. *NDT & E International*, **2020**, *110*, 102202.
10. Lu, M.; Meng, X.; Yin, W.; Qu, Z.; Wu, F.; Tang, J.; Xu, H.; Huang, R.; Chen, Z.; Zhao, Q.; Zhang, Z. Thickness measurement of non-magnetic steel plates using a novel planar triple-coil sensor. *NDT & E International*, **2019**, *107*, 102148.
11. Huang, R.; Lu, M.; Peyton, A.; Yin, W. Thickness measurement of metallic plates with finite planar dimension using eddy current method. *IEEE Transactions on Instrumentation and Measurement*, **2020**, *69*, 8424-8431.
12. Lu, M.; Meng, X.; Chen, L.; Huang, R.; Yin, W.; Peyton, A. Measurement of ferromagnetic slabs permeability based on a novel planar triple-coil sensor. *IEEE Sensors Journal*, **2019**, *20*, 2904-2910.
13. Lu, M.; Zhu, W.; Yin, L.; Peyton, A.; Yin, W.; Qu, Z. Reducing the lift-off effect on permeability measurement for magnetic plates from multifrequency induction data. *IEEE Transactions on Instrumentation and Measurement*, **2017**, *67*, 167-174.
14. Gallion, J.R.; Zoughi, R. Millimeter-wave imaging of surface-breaking cracks in steel with severe surface corrosion. *IEEE Transactions on Instrumentation and Measurement*, **2017**, 66, 2789-2791.
15. Tian, G.Y.; Sophian, A. Defect classification using a new feature for pulsed eddy current sensors. *NDT & E International*, **2005**, *38*, 77-82.

16. Luloff, M.S.; Morelli, J.; Krause, T.W. February. Examination of Dodd and Deeds solutions for a transmit-receive eddy current probe above a layered planar structure. *AIP Conference Proceedings*, *AIP Publishing LLC.*, **2017,** 1806, 110004.
17. Lu, M.; Huang, R.; Yin, W.; Zhao, Q.; Peyton, A. Measurement of permeability for ferrous metallic plates using a novel lift-off compensation technique on phase signature. *IEEE Sensors Journal*, **2019**, *19*, 7440-7446.
18. Betta, G.; Ferrigno, L.; Laracca, M. GMR-based ECT instrument for detection and characterization of crack on a planar specimen: A hand-held solution. *IEEE transactions on instrumentation and measurement*, **2011**, *61*, 505-512.
19. Huang, R.; Lu, M.; Peyton, A.; Yin, W. A novel perturbed matrix inversion based method for the acceleration of finite element analysis in crack-scanning eddy current NDT. *IEEE Access*, **2020**, *8*, 12438-12444.
20. Cannon, D.F.; Edel, K.O.; Grassie, S.L.; Sawley, K. Rail defects: an overview. *Fatigue & Fracture of Engineering Materials & Structures*, **2003**, *26*, 865-886.
21. Nicholson, G.L.; Davis, C.L. Modelling of the response of an ACFM sensor to rail and rail wheel RCF cracks. *NDT & E International*, **2012**, *46*, 107-114.
22. Bíró, O. Edge element formulations of eddy current problems. *Computer methods in applied mechanics and engineering*, **1999**, 169, 391-405.
23. Yin, W.; Lu, M.; Tang, J.; Zhao, Q.; Zhang, Z.; Li, K.; Han, Y.; Peyton, A. Custom edge-element FEM solver and its application to eddy-current simulation of realistic 2M-element human brain phantom. *Bioelectromagnetics*, **2018**, 39, 604-616.
24. Yin, W.; Lu, M.; Yin, L.; Zhao, Q.; Meng, X.; Zhang, Z.; Peyton, A. Acceleration of eddy current computation for scanning probes. *Insight-Non-Destructive Testing and Condition Monitoring*, **2018**, *60*, 547-555.
25. Yin, W.; Tang, J.; Lu, M.; Xu, H.; Huang, R.; Zhao, Q.; Zhang, Z.; Peyton, A. An equivalent-effect phenomenon in eddy current non-destructive testing of thin structures. *IEEE Access*, **2019**, *7*, 70296-70307.
26. Zeng, Z.; Udpa, L.; Udpa, S.S.; Chan, M.S.C. Reduced magnetic vector potential formulation in the finite element analysis of eddy current nondestructive testing. *IEEE transactions on magnetics*, **2009**, *45*, 964-967.
27. Papaelias, M.P.; Lugg, M.C.; Roberts, C.; Davis, C.L. High-speed inspection of rails using ACFM techniques. *NDT & E International*, **2009**, 42, 328-335.
28. Theodoulidis, T.; Poulakis, N.; Dragogias, A. Rapid computation of eddy current signals from narrow cracks. *NDT & E International*, **2010**, *43*, 13-19.
29. Theodoulidis, T. Analytical model for tilted coils in eddy-current nondestructive inspection. *IEEE transactions on magnetics*, **2005**, *41*, 2447-2454.
30. Dodd, C.V.; Deeds, W.E. Analytical solutions to eddy-current probe-coil problems. *Journal of applied physics*, **1968**, *39*, 2829-2838.
31. Harfield, N.; Bowler, J.R. Theory of thin-skin eddy-current interaction with surface cracks. *Journal of applied physics*, **1997**, *82*, 4590-4603.
32. Burke, S.K. Eddy-current inversion in the thin-skin limit: Determination of depth and opening for a long crack. *Journal of applied physics*, **1994**, *76*, 3072-3080.
33. Avila, J.R.S., Chen, Z., Xu, H. and Yin, W., 2018, May. A multi-frequency NDT system for imaging and detection of cracks. *2018 IEEE International Symposium on Circuits and Systems (ISCAS) IEEE*, **2018**, 1-4.
34. Xu, H.; Lu, M.; Avila, J.R.; Zhao, Q.; Zhou, F.; Meng, X.; Yin, W. Imaging a weld cross-section using a novel frequency feature in multi-frequency eddy current testing. *Insight-Non-Destructive Testing and Condition Monitoring*, **2019**, *61*, 738-743.
35. Yin, L.; Ye, B.; Rodriguez, S.; Leiva, R.; Meng, X.; Akid, R.; Yin, W.; Lu, M. Detection of corrosion pits based on an analytically optimised eddy current sensor. *Insight-Non-Destructive Testing and Condition Monitoring*, **2018**, *60*, 561-567.
36. Cheng, J.; Qiu, J.; Ji, H.; Wang, E.; Takagi, T.; Uchimoto, T. Application of low frequency ECT method in noncontact detection and visualization of CFRP material. *Composites Part B: Engineering*, **2017**, *110*, 141-152.
37. Cao, B.H.; Li, C.; Fan, M.B.; Ye, B.; Tian, G.Y. Analytical model of tilted driver–pickup coils for eddy current nondestructive evaluation. *Chinese Physics B*, **2018**, *27*, 030301.
38. Lu, M.; Xie, Y.; Zhu, W.; Peyton, A.; Yin, W. Determination of the magnetic permeability, electrical conductivity, and thickness of ferrite metallic plates using a multifrequency electromagnetic sensing system. *IEEE Transactions on Industrial Informatics*, **2018**, *15*, 4111-4119.

39. Lu, M.; Yin, L.; Peyton, A.; Yin, W. A novel compensation algorithm for thickness measurement immune to lift-off variations using eddy current method. *IEEE Transactions on Instrumentation and Measurement*, **2016**, *65*, 2773-2779.
40. Lu, M.; Chen, L.; Meng, X.; Huang, R.; Peyton, A.; Yin, W. Thickness measurement of metallic film based on a high-frequency feature of triple-coil electromagnetic eddy current sensor. *IEEE Transactions on Instrumentation and Measurement*, **2020**, *70*, 1-8.
41. Lu, M.; Meng, X.; Huang, R.; Chen, L.; Peyton, A.; Yin, W. Measuring lift-off distance and electromagnetic property of metal using dual-frequency linearity feature. *IEEE Transactions on Instrumentation and Measurement*, **2020**, *70*, 1-9.
42. Lu, M.; Meng, X.; Huang, R.; Chen, L.; Peyton, A.; Yin, W. Liftoff tolerant pancake eddy-current sensor for the thickness and spacing measurement of nonmagnetic plates. *IEEE Transactions on Instrumentation and Measurement*, **2020**, *70*, 1-9.
43. Huang, R.; Lu, M.; He, X.; Peyton, A.; Yin, W. Measuring Coaxial Hole Size of Finite-Size Metallic Disk Based on a Dual-Constraint Integration Feature Using Multifrequency Eddy Current Testing. *IEEE Transactions on Instrumentation and Measurement*, **2020**, *70*, 1-7.
44. W. Zhou, M. Lu, Z. Chen, L. Zhou, L. Yin, Q. Zhao, A. Peyton, Y. Li, W. Yin. "Three-Dimensional Electromagnetic Mixing Models for Dual-Phase Steel Microstructures." Applied Sciences, vol. 8, pp. 529, 2018.
45. M. Lu, R. Huang, W. Yin, Q. Zhao, A. Peyton, "Measurement of permeability for ferrous metallic plates using a novel lift-off compensation technique on phase signature." IEEE Sensors Journal, vol. 19, pp. 7440-7446, 2019.
46. M. Lu, H. Xu, W. Zhu, L. Yin et al. "Conductivity Lift-off Invariance and measurement of permeability for ferrite metallic plates," NDT & E International, vol. 95, pp. 36-44, Apr. 2018.
47. W. Yin et al. "Permeability invariance phenomenon and measurement of electrical conductivity for ferrite metallic plates," Insight-Non-Destructive Testing and Condition Monitoring, vol. 61, pp. 472-479, 2019.
48. M. Lu et al. "Determining the magnetic permeability of ferrite steel strip by a custom inversion method," Proc. 12th ECNDT, pp. 1-8, 2018.
49. M. Lu, et al. "Determination of the magnetic permeability, electrical conductivity, and thickness of ferrite metallic plates using a multi-frequency electromagnetic sensing system," IEEE Transactions on Industrial Informatics, vol. 15, pp. 4111-4119, 2019.
50. R. Huang, M. Lu et al, "Measurement of the radius of metallic plates based on a novel finite region eigenfunction expansion (FREE) method," IEEE Sensors Journal, vol. 20, pp. 15099 – 15106, 2020. Doi: 10.1109/JSEN.2020.3009443.
51. R. Huang, M. Lu et al, "Measuring co-axial hole size of finite-size metallic disk based on a dual-constraint integration feature using multi-frequency eddy current testing," IEEE Transactions on Instrumentation and Measurement, vol. 70, pp. 1-7, 2020. Doi: 10.1109/TIM.2020.3026762.
52. M. Lu et al, "Lift-off tolerant pancake eddy-current sensor for the thickness and spacing measurement of non-magnetic plates," IEEE Transactions on Instrumentation and Measurement, early access, 2020. Doi: 10.1109/TIM.2020.3033377.
53. M. Lu et al, "Inversion of distance and magnetic permeability based on material-independent and lift-off insensitive algorithms using eddy current sensor," IEEE Transactions on Instrumentation and Measurement, early access, 2020. Doi: 10.1109/TIM.2020.3036099.
54. W. Yin et al, "Measurements of Thickness for Metallic Plates With Co-Axial Holes Using a Novel Analytical Method With the Modified Integration Range," IEEE Access, vol. 8, pp. 198301 – 198306, 2020.
55. X. Meng, M. Lu et al, "Inversion of lift-off distance and thickness for non-magnetic metal using eddy current testing," IEEE Transactions on Instrumentation and Measurement, vol. 70, 2020. Doi: 10.1109/TIM.2020.3038289.
56. M. Lu, X. Meng, et al, "Determination of surface crack orientation based on thin-skin regime using triple-coil drive-pickup eddy-current sensor," IEEE Transactions on Instrumentation and Measurement, early access, 2020. Doi: 10.1109/TIM.2020.3044729.
57. Yin, W.; Tang, J.; Lu, M.; et al. An equivalent-effect phenomenon in eddy current non-destructive testing of thin structures. IEEE Access, 2019, 7, pp. 70296-70307.
58. Lu, M.; et al. Determination of Surface Crack Orientation Based on Thin-Skin Regime Using Triple-Coil Drive–Pickup Eddy-Current Sensor. IEEE Transactions on Instrumentation and Measurement, 2020, 70, pp. 1-9. DOI: 10.1109/TIM.2020.3044729

59. M. Lu, et al., "Prediction of the asymptotical magnetic polarization tensors for cylindrical samples using the boundary element method," In 2015 IEEE Sensors Applications Symposium (SAS), pp. 1-4. IEEE, 2015.
60. R. Huang, M. Lu, A. Peyton, and W. Yin, "A novel perturbed matrix inversion based method for the acceleration of finite element analysis in crack-scanning eddy current NDT," IEEE Access, vol. 8, pp. 12438-12444, 2020.
61. J. Tang et al., "A Novel Efficient FEM Thin Shell Model for Bio-Impedance Analysis," Biosensors, vol. 10, no. 6, pp. 69, 2020.
62. L. Chen, et al., "Textile Based Capacitive Sensor for Physical Rehabilitation via Surface Topological Modification," ACS Nano, vol. 14, no. 7, pp. 8191-8201, 2020. DOI: 10.1021/acsnano.0c01643
63. Z. Jin, et al., "Methods of Controlling Lift-off in Conductivity Invariance Phenomenon for Eddy Current Testing," IEEE ACCESS, vol. 8, pp. 2169-3536, 2020. DOI: 10.1109/ACCESS.2020.3007216.
64. J. Tang, et al., "Effect of frozen-thaw injury on cell membrane and bio-impedance," In 2020 IEEE International Instrumentation and Measurement Technology Conference (I2MTC), pp. 1-6. IEEE, 2020.
65. J. Tang, et al., "Bio-impedance spectroscopy for frozen-thaw of bio-samples: Non-contact inductive measurement and finite element (FE) based cell modelling," Journal of Food Engineering, vol. 272, pp. 109784, 2020.
66. H. Xu et al., "Imaging a weld cross-section using a novel frequency feature in multi-frequency eddy current testing," Insight-Non-Destructive Testing and Condition Monitoring, vol. 61, no. 12, pp. 738 - 743, 2019.
67. Y. Xie et al., "Novel Wearable Sensors for Biomechanical Movement Monitoring Based on Electromagnetic Sensing Techniques," IEEE Sensors Journal, vol. 20, no. 2, 2020. DOI: 10.1109/JSEN.2019.2943487
68. W. Yin et al., "Permeability invariance phenomenon and measurement of electrical conductivity for ferrite metallic plates," Insight-Non-Destructive Testing and Condition Monitoring, vol. 61, no. 8, pp. 472 - 479, 2019.
69. M. Lu et al., "A model for the triboelectric nanogenerator with inductive load and its energy boost potential," Nano Energy, vol. 63, pp. 103883, 2019.
70. M. Lu et al., "Forward solver for deep earth exploration and induction logging using custom built Edge-Element FEM technique," Acta Geologica Sinica, vol. 93, pp. 302-304, 2019.
71. L. Chen et al., "Whole System Design of Wearable Magnetic Induction Sensor for Physical Rehabilitation," Advanced Intelligent Systems, vol. 1, no. 1, pp. 1900037, 2019.
72. Y. X et al., "A self-powered radio frequency (RF) transmission system based on the combination of triboelectric nanogenerator (TENG) and piezoelectric element for disaster rescue/relief," Nano Energy, vol. 54, pp. 331-340, 2018.
73. W. Yin et al., "Custom edge-element FEM solver and its application to eddy-current simulation of realistic 2M-element human brain phantom," Bioelectromagnetics, vol. 39, no. 8, pp. 604-616, 2018.
74. L. Yin et al., "Detection of corrosion pits based on an analytically optimised eddy current sensor," Insight-Non-Destructive Testing and Condition Monitoring, vol. 60, no. 10, pp. 561-567, 2018.
75. W. Yin et al., "Acceleration of eddy current computation for scanning probes," Insight-Non-Destructive Testing and Condition Monitoring, vol. 60, no. 10, pp. 547-555, 2018.
76. W. Zhou et al., "Three-dimensional electromagnetic mixing models for dual-phase steel microstructures," Applied Sciences, vol. 8, no. 4, pp. 547-555, 2018.
77. M. Lu, et al., "Determining the magnetic permeability of ferrite steel strip by a custom inversion method," In Proc. 12th ECNDT, pp. 1-8. 2018.
78. J. Tang, et al., "Cellular structure analysis based on magnetic induction finite element method simulations and measurements," bioRxiv, pp. 275271, 2018. DOI: 10.1101/275271
79. J.R.S. Avila, et al., "A novel dual modality sensor with sensitivities to permittivity, conductivity, and permeability," IEEE Sensors Journal, vol. 18, no. 1, pp. 356-362, 2017.
80. T. Yang, et al., "Level measurement for saline with a small surface area using high frequency electromagnetic sensing technique," Measurement, vol. 101, pp. 118-125, 2017.
81. X. Meng, et al, "Evaluation of coating thickness using lift-off insensitivity of eddy current sensor," Sensors, vol. 21, no. 2, pp. 419, 2021.
82. Meng, X.; Lu, M.; Yin, W.; Bennecer, A.; Kirk, K.J. Evaluation of Coating Thickness Using Lift-Off Insensitivity of Eddy Current Sensor. Sensors 2021, 21, 419. https://doi.org/10.3390/s21020419
83. M. Lu, et al., "Thickness measurement of circular metallic film using single-frequency eddy current sensor," NDT & E International, vol. 119, pp. 102420, 2021.

84. G. Hu, et al., "Measurement of Radius of a Metallic Ball Using Eddy Current Testing Based on Peak Frequency Difference Feature," Measurement, vol. 184, pp. 109876, 2021.
85. Y. Xie, et al., " A novel design of window function modulated meander-line-coils EMATs for unidirectional Rayleigh waves generation and sidelobes suppression," NDT & E International, vol. 123, pp. 102501, 2021.
86. M. Lu, et al., "Lift-off invariant inductance of steels in multi-frequency eddy-current testing." NDT & E International, vol. 121, p. 102458, 2021.
87. Z. Jin, et al., "Boundary-element analysis of magnetic polarization tensor for metallic cylinder." IEEE Access, vol. 9, pp. 63250-63256, 2021
88. M. Lu, et al., " A high-frequency phase feature for the measurement of magnetic permeability using eddy current sensor." NDT & E International, pp. 102519, 2021, ISSN 0963-8695, https://doi.org/10.1016/j.ndteint.2021.102519.
89. Lu, M.; Meng, X.; Huang, R.; Chen, L.; Peyton, A.; Yin, W. A High-Frequency Phase Feature for the Measurement of Magnetic Permeability Using Eddy Current Sensor. Preprints 2021, 2021080154 (doi: 10.20944/preprints202108.0154.v1)
90. Lu, M, Yin, W & Peyton, A 2015, A custom edge-element FEM solver for eddy current NDT. in 54th Annual British Conference of Non-Destructive Testing, NDT 2015. British Institute of Non-Destructive Testing, 54th Annual British Conference of Non-Destructive Testing, Telford, United Kingdom, 8/09/15.
91. Lu, Mingyang, Noushin Karimian, Anthony Peyton, and Wuliang Yin. "Acceleration of Sweeping Frequency in Eddy Current Computation." In 55th Annual Conference of the British Institute of Non-Destructive Testing, pp. 494-507. British Institute of Non-Destructive Testing, 2016.
92. Lu, Mingyang. Forward and inverse analysis for non-destructive testing based on electromagnetic computation methods. The University of Manchester (United Kingdom), 2018.
93. Lu, M. "Inversion analysis of the spectra of a multi-frequency electromagnetic sensor to determine the magnetic permeability, electrical conductivity and thickness of steel strip." Forward and inverse analysis for non-destructive testing based on electromagnetic computation methods: 102.
94. Lu, M. "Conductivity Lift-off Invariance and measurement of permeability for magnetic plates." Forward and inverse analysis for non-destructive testing based on electromagnetic computation methods: 78.
95. Lu, M. "Acceleration of Eddy Current Computation for Scanning Probes." Forward and inverse analysis for non-destructive testing based on electromagnetic computation methods (2018): 34.
96. Zhu, Shuang, Jorge R. Salas Avila, Yang Tao, Yuedong Xie, Anthony J. Peyton, Jialuo Ding, Stewart Williams, Wuliang Yin, and Mingyang Lu. "Measurement of electrical conductivity for metal wires using an electromagnetic sensor." In 57th Annual Conference of the British Institute of Non-Destructive Testing, pp. 40-48. 2018.
97. Lu, Mingyang, Wenqian Zhu, Wuliang Yin, Frenk Van Den Berg, Haibing Yang, and Anthony Peyton. "12th European Conference on Non-Destructive Testing (ECNDT 2018)." In Determining the magnetic permeability of ferrite steel strip by a custom inversion method. 2018.
98. Karimian, Noushin, Mingyang Lu, John W. Wilson, Wuliang Yin, and Anthony J. Peyton. "Defect representation using the electromagnetic tensor formulation for Eddy Current NDT." In 55th Annual Conference of the British Institute of Non-Destructive Testing, pp. 441-450. British Institute of Non-Destructive Testing, 2016.
99. Xie, Yuedong, Jun Long, Pengfei Zhao, Jinkai Chen, Jikui Luo, Zhijie Zhang, Kai Li et al. "A self-powered radio frequency (RF) transmission system based on the combination of triboelectric nanogenerator (TENG) and piezoelectric element for disaster rescue/relief." Nano Energy 54 (2018): 331-340.